nature communications

Article

https://doi.org/10.1038/s41467-026-70756-x

IVNS1ABP mutation drives cellular senescence in newly identified progeroid neuropathy

Received: 13 January 2025

Accepted: 3 March 2026

Published online: 19 March 2026

Check for updates

Fang Yuan[1,2,3], Ye Sing Tan[1,2], Haofei Wang[4], Ain Nur Ali[5], Qiang Yuan[1,2], Shu-Min Chou[1,2], Yu-Hsin Yen[1,2], Gunaseelan Narayanan[1], Lei Zhou[6], Mohammad Shboul[7], Carine Bonnard[8,9], Bruno Reversade[5,10,11,12] & Su-Chun Zhang[1,2,3]

We identified a new progeroid syndrome with severe neuropathy and intellectual deficits but its underlying cellular and molecular mechanism is unknown. Exome sequencing revealed a homozygous mutation in the *IVNS1ABP* gene, which encodes IVNS1ABP, an influenza virus non-structural protein-1 binding protein. To investigate disease mechanisms, we generated isogenic induced pluripotent stem cells (iPSCs) from patient fibroblasts and differentiated them into neural progenitor cells (NPCs). Mutant IVNS1ABP fibroblasts, iPSCs, and NPCs exhibited defective cytokinesis, increased DNA damage, and premature cellular senescence. Consistent with these findings, cerebral organoids showed early differentiation of NPCs into neurons. Molecular profiling as well as biochemical and cellular analysis revealed altered binding of mutant IVNS1ABP to actin / actin-associated proteins and dysregulated actin dynamics during cytokinesis. Taken together, we propose that mutant IVNS1ABP dysregulates actin polymerization and organization which is at least partly responsible for the cellular senescence phenotypes in this progeroid neuropathy.

Cellular senescence occurs throughout life, contributing to development or aging[1]. Mitotic cells undergoing senescence display telomere attrition, DNA damage, increased levels of senescence-associated β-galactosidase (SA-β-Gal), dysregulated metabolism, accumulation of macromolecule aggregates, and senescence-associated secretory phenotypes (SASP)[2]. The causes of cellular senescence are diverse, resulting in highly heterogeneous and dynamic senescence outcomes.

During development, errors in mitotic control can promote genomic instability, aneuploidy, and cytokinesis failure, which in turn can drive senescence and premature aging[3–5]. For instance, reduction of the spindle assembly checkpoint (SAC) protein BubR1 increases

[1]Program in Neuroscience & Behavioral Disorders, Duke-NUS Medical School, Singapore, Singapore. [2]GK Goh Centre for Neuroscience, Duke-NUS Medical School, Singapore, Singapore. [3]Center for Neurologic Diseases, Sanford Burnham Prebys Medical Discovery Institute, La Jolla, CA, USA. [4]The McAllister Heart Institute, The University of North Carolina at Chapel Hill, Chapel Hill, NC, USA. [5]Genome Institute of Singapore (GIS), Agency for Science, Technology and Research (A*STAR), Singapore, Singapore. [6]School of Optometry; Department of Applied Biology and Chemical Technology; Research Centre for SHARP Vision (RCSV), The Hong Kong Polytechnic University, Hong Kong, China. [7]Department of Medical Laboratory Sciences, Jordan University of Science and Technology, Irbid, Jordan. [8]Model Development, A*STAR Skin Research Labs (A*SRL), Agency for Science, Technology and Research (A*STAR), Singapore, Singapore. [9]Asian Skin Biobank, Skin Research Institute of Singapore (SRIS), Agency for Science, Technology and Research (A*STAR), Singapore, Singapore. [10]Department of Medical Genetics, Koç University School of Medicine, Istanbul, Turkey. [11]Department of Physiology, Yong Loo Lin School of Medicine, National University of Singapore, Singapore, Singapore. [12]Biological, Environmental Sciences and Engineering (BESE), King Abdullah University of Science and Technology (KAUST), Thuwal, Saudi Arabia. e-mail: suchunz@sbpdiscovery.org

aneuploidy and senescence in mammals[6]. BubR1 mutant mice showed progeroid features, including short lifespan, cachectic dwarfism, lordokyphosis, cataracts, loss of subcutaneous fat and impaired wound healing[7]. In Hutchinson-Gilford Progeria Syndrome (HGPS), mutated lamin A produces a truncated protein progerin, which accelerates cellular senescence by forming abnormal nuclear structures, disrupting cell division and inducing telomere dysfunction[8,9]. The expression of progerin is also detected during the normal aging process[10], suggesting shared mechanisms between premature aging and physiological aging. However, segmental progeria syndromes do not fully capture the aging process as cognitive functions are often well-preserved in these conditions[11,12].

In this context, we identified an undiagnosed progeroid syndrome in a family whose adolescent members displayed early-onset aging features[13]. Clinical manifestations include progressive skin dyschromatosis, presenting as both hypo- and hyperpigmented macules distributed across the face and body. Additional features include premature graying of scalp hair, eyelashes, and eyebrows. A striking feature is progressive motor and gait impairment, as well as intellectual disability, which is coupled with a thinner corpus callosum and cerebellar vermis[13]. The extent and severity of symptoms increased with age[13]. We hence refer to this disease as "progeroid neuropathy". Exome sequencing coupled to homozygosity mapping revealed a germline homozygous variant p.F253C in the *IVNS1ABP* gene, which encodes NS1-BP, an influenza virus non-structural protein-1 binding protein. This variant has never been reported according to publicly available databases[13]. The gene is mainly known for mediating RNA splicing and mRNA export during the influenza virus transfection process[14,15]. Structurally, IVNS1ABP is a Kelch protein, belonging to the Kelch-like (KLHL) subfamily of proteins that function as adapters for the E3 ligases. Unlike most KLHL proteins, which bind Cullin3, IVNS1ABP appears to regulate the proteasome system indirectly through KLHL20[16]. IVNS1ABP has also been found to stabilize F-actin organization in a fibroblast cell line by binding to actin through its Kelch repeats[17,18]. It is also postulated as a risk gene for primary immunodeficiency in a recent WGS study[19]. Although the mouse ortholog of IVNS1ABP has been implicated in fibroblast proliferation[18], IVNS1ABP itself has not been associated with aging, and its contribution to premature aging and neuropathy is unknown.

Here, we acquired dermal fibroblasts from the patients and their family members, generated isogenic iPSCs from the fibroblasts and differentiated the isogenic iPSCs to NPCs. To investigate how aging happens at the cellular level, we focus on the senescence phenotypes. We found that the fibroblasts, iPSCs, and NPCs with the IVNS1ABP mutation exhibited hallmark features of senescence. Mutant cells proliferated more slowly, showed a lengthened cell cycle, and frequently displayed cytokinesis defects and mitotic failure. Proteomics analyses indicated reduced binding of mutant IVNS1ABP to actin and actin-binding proteins, leading to impaired actin polymerization. We propose that dysregulated actin organization contributes to cellular senescence and premature neural differentiation in this progeroid neuropathy.

Results

Mutant IVNS1ABP NPCs display increased DNA damage and cellular senescence

Since no model systems were available for the newly identified disease, we generated three iPSC cell lines from dermal fibroblasts of the siblings, two from siblings 1 and 4 carrying a homozygous missense p.(Phe253Cys) variant at an intervening region (IVR) between the BACK domain and Kelch domain of IVNS1ABP and one from the non-affected sibling 2 (Fig. 1A). To investigate the potential roles of IVNS1ABP and reduce the variations derived from different genetic backgrounds, we established three isogenic iPSC pairs by CRISPR/Cas9 (Fig. 1B and Fig. S1A). Pair I (Ctrl_I and MT_I) and Pair III (Ctrl_III and MT_III) were generated from two patient siblings by correcting the mutation site, and Pair II (Ctrl_II and MT_II) were generated from the unaffected sibling by knocking in the same mutation (Fig. 1B and Fig. S1A, B). Additionally, we generated an IVNS1ABP knockout (KO) line in Pair III (Fig. 1B and Fig. S1B, C). The identity and authenticity of these iPSC lines were verified by PCR, Sanger sequencing, off-target analysis and karyotyping, as well as the expression of pluripotency markers NANOG and TRA-1-60 (Fig. S1B–D).

Since the patients showed severe neurological and cognitive symptoms as well as premature aging signs, we differentiated the isogenic pairs of iPSCs to forebrain NPCs, following our established protocol[20]. The identity of NPCs was confirmed by their positive immunostaining for the neuroepithelial stem cell marker NESTIN (Fig. 1C). Quantitative analysis showed a similar proportion of NESTIN+ NPCs between the mutant and isogenic groups at day 10 (Fig. 1G), demonstrating that the neural differentiation capacity at this early developmental stage is not affected by the IVNS1ABP$^{F253C/F253C}$ mutation.

Cellular senescence is often caused or accompanied by DNA damage[21]. Consistent with this, both IVNS1ABP$^{F253C/F253C}$ mutant (MT) and IVNS1ABP$^{KO/KO}$ (KO) NPCs showed more γH2AX foci, which is phosphorylation of the Ser-139 residue of the histone variant H2AX, indicating a DNA damage event, as compared to the isogenic controls (Fig. 1D, H). Histone H3 trimethyl Lys9 (H3K9me3), a heterochromatin mark associated with chromatin integrity, showed decreased expression in MT and KO NPCs as compared to the control groups (Fig. 1E, I). In addition, the nuclear content of the IVNS1ABP MT cells was increased (Fig. 1J). To further confirm the senescence phenotype, we performed SA- β-Gal staining on NPCs derived from the three isogenic iPSC pairs. SA-β-Gal activity is a widely used histochemical marker for detecting cellular senescence due to its increased lysosomal β-galactosidase activity at pH 6.0. Both MT NPCs and KO NPCs showed an increased proportion of SA-β-Gal active cells (Fig. 1F, K). The expression level of Cyclin-dependent kinase inhibitor 2 A (CDKN2A/p16), a cell cycle repressor and signature cellular senescence marker, was increased in the IVNS1ABP$^{F253C/F253C}$ NPCs compared to the isogenic controls (Fig. 1L).In addition, IVNS1ABP protein levels were reduced in the mutant NPCs than in the control NPCs in all three isogenic pairs, suggesting that the downregulation of its protein expression and potential loss-of-function (Fig. 1M). Taken together, our results demonstrate that IVNS1ABP MT NPCs undergo marked cellular senescence.

Transcriptomics profiling reveals mitotic misregulation in IVNS1ABP MT NPCs

Senescence phenotypes are highly heterogeneous and dynamic. To systematically explore the cellular senescence caused by IVNS1ABP$^{F253C/F253C}$, RNA-sequencing (RNA-seq) was performed on iPSC and NPC from isogenic pair III (Ctrl, MT and KO) (three biological replicates per condition) (Fig. 2A). Principal component analysis (PCA) showed that NPC samples were clustered separately from the iPSC samples (Fig. 2B), suggesting cell type-specific gene expression differences. The iPSC samples were clustered together, whereas the MT/KO NPCs were segregated from the control NPCs (Fig. 2B), suggesting that the impact of MT IVNS1ABP is primarily on somatic cells. Moreover, MT NPC samples clustered close to KO NPC samples, indicating transcriptomic similarities between MT and KO. Similar to the PCA plot, sample-to-sample correlation analysis showed that MT NPCs presented a close correlation with KO NPCs (Fig. 2C), suggesting that the mutation behaves as a loss-of-function allele.

To assess the senescence phenotypes in a comprehensive manner, we performed gene enrichment analysis (GSEA) with Gene Ontology terms relating to the cellular phenotypes we observed, including GO terms from DNA damage response (DDR), apoptosis, cell cycle regulation, inflammatory signaling, metabolic pathways

https://doi.org/10.1038/s41467-026-70756-x

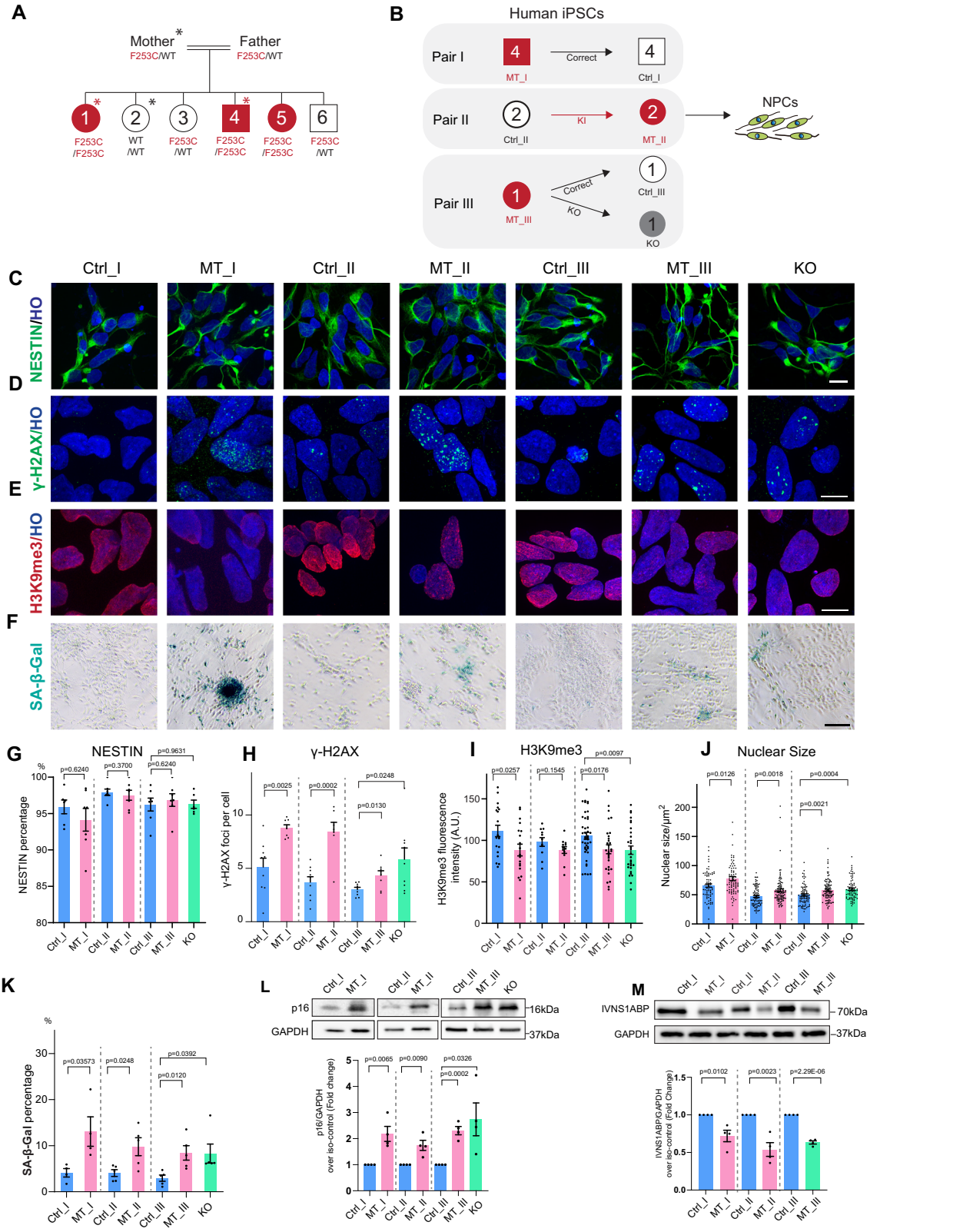

(mitochondrial function, oxidative stress response, etc). Cellular senescence was the GO term with the highest enrichment score and showed higher expression levels of genes in MT NPCs than Ctrl NPCs, as well as KO NPCs (Fig. 2D and Fig. S2C–E). Among these upregulated genes were several well-established senescence-associated regulators, such as *TP53*, *CDKN1A*, *CDKN2A*, *CDKN1B*, and *CDKN2B* (Fig. 2E and S2D). These genes are highly involved in the regulation of cell cycle arrest and are commonly activated in response to cellular stress, contributing to the senescence phenotype[22]. To further confirm the upregulation of these genes, we validated mRNA expression of *CDKN1A*, *CDKN2B* and CDKN2A in all three isogenic pairs, which showed a consistent trend (Fig. S2E).

We then performed weighted gene co-expression network analysis (WGCNA) to investigate gene sets that are similarly affected by the

Fig. 1 | MT IVNS1ABP NPCs display DNA damage and cellular senescence. **A** Family tree of the mutation in *IVNS1ABP*. Red color indicates affected patients. * marks the individual origin of primary fibroblasts, including a heterozygous healthy mother, one non-affected healthy sibling and two homozygous mutation siblings. **B** Graphic flow for disease modeling. Three isogenic iPSCs were generated from one non-affected healthy sibling, two siblings with the homozygous mutation were reprogrammed to iPSCs, and then the isogenic lines, as well as IVNS1ABP KO isogenic iPSCs, were generated. The number on the individual indicates the sibling referred to in the family tree graph (**A**). **C** Representative images of NESTIN+ NPCs derived from all three isogenic pairs of iPSCs. Scale bar, 50 µm. **D**, **E** Representative images of γH2AX (**D**) and H3K9me3 (**E**) staining in NPCs. Scale bar, 10 µm. **F** Representative images of SA-β-Gal staining on three isogenic iPSCs derived NPCs. Scale bar, 50 µm. **G** Quantification of NESTIN+ iPSC-derived NPCs in (**C**). Cells were quantified at day 10 to evaluate the neural lineage differentiation potential. Total cell numbers were $n = 749$, 502, 404, 553, 615, 414, and 458 from three independent cultures. **H**, **I** Quantification of γH2AX foci (**D**) and H3K9me3 intensity (**E**). Total cell numbers of γH2AX foci were $n = 144$, 110,156, 124, 157, 196, and 153 from three independent cultures. H3K9me3 intensity were quantified with >10 randomly choosen fields from three independent cultures. Fluorescence intensity is shown in arbitrary units (AU). **J** Quantification of nuclear size in iPSC-derived NPCs. Total cell numbers $n = 80$, 101, 70, 80, 82, 99, and 78 from three independent cultures. **K** Quantification of SA-β-Gal percentage (**F**) in total cells. Total cell numbers were $n = 1393$, 1073, 1003, 1145, 1865, 2181, and 1442 from three independent cultures. **L** Immunoblot and quantification for p16 in NPCs derived from isogenic pair I, II, and III, $n = 4$ independent cultures. **M** Immunoblot and quantification for IVNS1ABP in NPCs derived from isogenic pair I, II, and III; $n = 4$ independent cultures. Statistical comparisons were performed using unpaired two-tailed Student's *t*-tests for each isogenic cell line pair ($n = 3$ pairs). Each pair was analyzed separately for comparison between the two cell lines within each isogenic background. Data were presented as mean values ± SEM. Source data are provided as a Source Data file.

IVNS1ABP mutation. Module-trait analysis of WGCNA identified 39 co-expression modules, of which 9 modules showed differentially correlated gene expression patterns between WT NPCs and MT NPCs ($p < 1e\text{-}7$) (Fig. 2F and Fig. S1A and S2B). The top four module eigengenes (MEyellow, MEgreen, MEblue, and MEtan) were processed by GO analysis. The yellow module showed enrichment in embryonic development-related terms, while the blue and green modules were enriched in neuron-related terms and metabolism-related terms, respectively (Fig. 2F). Of note, the tan module showed a distinct expression pattern both in the iPSC stage and NPC stage. It was enriched in mitotic-related terms, including chromosome segregation (GO: 0007059) and mitotic cell cycle phase transition (GO: 0044772) (Fig. 2F), corresponding to the senescence phenotypes (Fig. 1) and suggesting cell cycle dysregulation as a potential underlying cause.

At the cellular level, immunostaining for α-Tubulin (mitotic spindle marker) and pericentrin (centrosome marker), revealed several cell division abnormalities, including multipolar division, micronuclei, lagging chromosomes, monopolar spindle and misaligned spindles (Fig. 2G and Fig. S2G). The incidence of abnormal divisions in the IVNS1ABP MT and KO cells was significantly higher than that of the isogenic control group in all three isogenic pairs (Fig. 2H), indicating mitotic failure in IVNS1ABP MT NPCs.

Cell cycle arrest mediates mutant IVNS1ABP-induced senescence

The change in transcriptional profiles of cell cycle regulators and misalignment of chromosomes during mitosis suggest cell cycle arrest as a mediator of cellular senescence in IVNS1ABP MT cells. Consistent with this, we observed that the patient's fibroblasts, iPSCs, and NPCs grew more slowly than the unaffected cells (Fig. S3A), which is likely caused by reduced proliferation. Using cell proliferation assay, with 18 h pulse of 5-ethynyl-2'-deoxyuridine (EdU) to label S-phase cells, we showed a reduced proportion of EdU-positive cells in the IVNS1ABP MT fibroblasts as compared to the unaffected controls (Fig. 3A, B). The expression of Ki67, a marker for proliferation, also decreased in patient fibroblasts (Fig. 3A, B and Fig. S3B).

Using isogenic pairs for rigorous comparison, we found that the proportion of EdU-positive cells in the patient and KO iPSCs was significantly lower (Fig. 3C, E and Fig. S3C), consistent with our observation that the patient iPSCs formed smaller colonies and took longer to reach confluency. NPCs also showed a decreased proportion of EdU-positive cells in the MT and KO groups compared with their isogenic groups (Fig. 3D, F). These results demonstrate that the reduced proliferation is a general defect of the IVNS1ABP mutation, with correction of the mutation restoring the cell proliferation capacity. Detection of cell death by cleaved caspase-3 staining showed an increased proportion of positive cells in IVNS1ABP$^{F253C/F253C}$ MT and KO NPCs (Fig. S4A, B). Thus, the reduced growth rate is general to many cell types and is caused by both reduced proliferation and increased cell death.

To gain mechanistic insights into the reduction of cell proliferation, we examined the cell cycle program of iPSCs using the FUCCI system with live cell imaging. FUCCI, a Fluorescent Ubiquitination-based Cell Cycle Indicator[23], reports the G_1 and S/G2 phases by red and green fluorescent reporters in the nucleus, respectively, and the M phase by nuclear envelope breakdown and morphological changes (Fig. 3G). The iPSCs were chosen for the FUCCI assay as they are highly homogeneous and possess a relatively shorter division time[24]. We found that the whole cell cycle duration became longer in IVNS1ABP MT cells than in the isogenic control cells (Isogenic pair I: 26 h Ctrl vs. 34 h MT; Isogenic pair II: 13 h Ctrl vs. 16 h MT; Isogenic pair III: 13 h Ctrl vs. 29 h MT) (Fig. S5 and Supplementary Video 1). Almost all the cell cycle phases were prolonged in the IVNS1ABP MT and KO cells (Fig. 3H). Cell death was also observed during live cell imaging of the FUCCI assay, wherein some cells underwent uneven cell division, followed by shrinkage and disappearance of the daughter cells (Fig. S4C). These mitotic failures explain the increased cell death revealed by Caspase-3 staining (Fig. S4S, B). These results suggest mitotic misregulation as a crucial cause for MT IVNS1ABP-induced cell cycle arrest, DNA damage, and cellular senescence.

Cell cycle dysregulation is accompanied by premature differentiation in MT IVNS1ABP cerebral organoids

Our patients display severe neurological symptoms and intellectual delay, suggesting the impact of MT IVNS1ABP on neural development and/or maintenance. The cell cycle dysregulation in NPCs would impair developmental programs such as proliferation and/or differentiation. To gain insights into the role of IVNS1ABP in regulating neural development, we generated cerebral organoids from isogenic iPSC lines in addition to 2D cultures of NPCs (Fig. 4A). The measurement of organoid size at 5 weeks showed an apparent reduction in MT and KO organoid size, compared to their isogenic control (Fig. 4B, C and Fig. S6B). In both MT and isogenic control organoids, SOX2-expressing cells around the lumen divided and radially lined up, resembling the ventricular zone (VZ) of the developing cerebral cortex (Fig. 4B and Fig. S6C). Similar to our observations in 2D cultures of NPCs (Fig. 3D, F), both SOX2 and Ki67 proportions were reduced in MT organoids compared to isogenic control organoids (Fig. 4B, D, E), indicating that the NPC exits the cell cycle earlier in IVNS1ABP MT organoids. This early cell cycle exit was accompanied by increased DNA damage, indicated by γH2AX foci and cell death, marked by cleaved caspase-3 staining (Fig. S6E, F), consistent with the observations in NPCs (Fig. S4A, B).

Earlier cell cycle exit would alter the cell differentiation program. Indeed, in a 2D neural differentiation culture system, we found early appearance of Doublecortin (DCX, newborn neuron marker) neurons in both MT and KO NPCs at day 10, which normally occurs two weeks after differentiation in normal iPSCs (Fig. 4F and Fig. S6A). This premature differentiation indicates a shift in the developmental program. In

https://doi.org/10.1038/s41467-026-70756-x

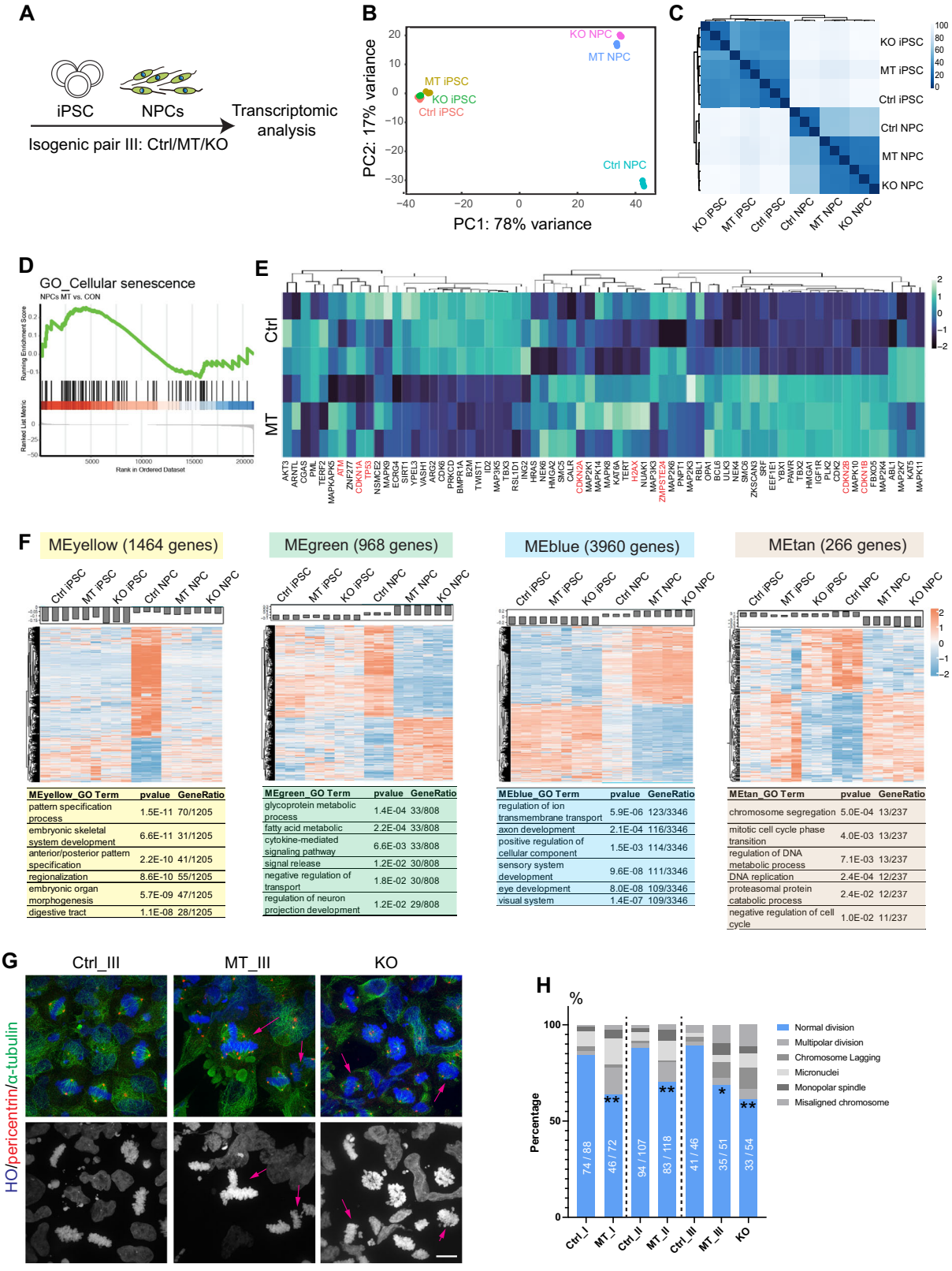

cerebral organoids, NPCs differentiate to postmitotic neurons following their intrinsic temporal course, presenting a platform to assess if the neural development is altered by MT IVNS1ABP. Indeed, the area covered by DCX+ neurons and neurites was much larger in the MT organoid than in the isogenic organoid at 3 weeks (Fig. 4G). By 5 weeks, the population of maturing neurons, marked by Neuronal Nuclei (NeuN), was significantly higher in MT than in the isogenic organoids (Fig. 4H, I).

To further confirm the premature shift in neural development, we assessed 8-week-old cerebral organoids. The MT organoid size was still smaller than its isogenic control (Fig. 4K). At this time point, the organoid structure was relatively clear with SOX2-expressing NPCs representing the VZ area and βIII-tubulin-expressing neurons and their neurites representing the SVZ area. The VZ-like area was thinner while the SVZ-like area was thicker in the MT organoids as compared to their

Fig. 2 | Mitotic misregulation in MT NPCs by RNA-sequencing and immunostaining. A Schematic flow chart of transcriptomics analysis. **B** Principal component analysis (PCA) plot showing sample clustering and variance. **C** A heat map showing sample-to-sample distances by hierarchical clustering using DESeq2 based on Poisson distance (blue signifies a high correlation). **D** GSEA plots showing cellular senescence in NPCs, MT vs. Ctrl, enrichment score = 0.89. **E** Heat map depicting cellular senescence-related gene expression in Ctrl and MT NPCs, genes in red are senescence core genes. **F** Heat map and GO analysis of eigengenes in the top four modules. **G** Representative images shown mitotic spindle defects in MT/KO NPCs in isogenic Pair III. Metaphase cells were stained with α-tubulin (spindle) and pericentrin (centrosome) at the top; the bottom panel showed the nucleus staining. Pink arrows point to the abnormal division. Scale bar, 10 μm. **H** Quantification showing the percentage of abnormal division, including multipolar division, chromosome lagging, micronuclei, monopolar spindle, and misaligned chromosomes in all three isogenic iPSCs derived NPCs, respectively. Data were collected from three independent cultures in each cell line and *n* number in each group was indicated on the bar graph. Quantification was performed by calculating the proportion of normal division events for each cell line, followed by statistical comparison of proportions between groups using Fisher's exact test. $p_{Ctrl\_I\ vs.\ MT\_I} = 0.0055$ (**), $p_{Ctrl\_II\ vs.\ MT\_II} = 0.0018$(**), $p_{Ctrl\_III\ vs.\ MT\_III} = 0.0248$ (*), $p_{Ctrl\_III\ vs.\ KO} = 0.0015$ (**). Statistical comparisons: unpaired two-tailed *t*-tests for each isogenic cell line pair. Source data are provided as a Source Data file.

isogenic counterparts (Fig. 4J, L). In particular, the βIII-tubulin-positive postmitotic neurons were present at the VZ-like area besides the SVZ-like area in the MT organoids, whereas they were present mainly in the SVZ-like area in the isogenic organoids at 8 weeks (Fig. 4J, M). Similar results were observed in isogenic pair III, including KO organoids (Fig. S6C, D). Besides, this developmental shift was also revealed by staining for COUP-TF-interacting protein 2 (CTIP2) and T-box brain protein 2 (TBR2). TBR2 is generally taken as a subventricular zone (SVZ) progenitor marker while CTIP2 marks deep-layer mature neurons. MT organoids exhibited a significantly higher proportion of CTIP2+ cells and reduced TBR2+ cells, indicating an altered developmental program (Fig. S6G, H). CTIP2+ cells largely co-expressed TBR2 in Ctrl organoids, suggesting a transitioning state from progenitors to neurons. In contrast, most of the CTIP2+ cells were TBR2- in MT organoids, suggesting these cells had already bypassed the transition stage (Fig. S6G).

These results highlight the premature neuronal differentiation accompanying MT IVNS1ABP-associated cell cycle dysregulation, at least partly explaining the neurological and intellectual deficits.

IVNS1ABP mutation alters its binding to and polymerization of actin

IVNS1ABP structurally belongs to the adapter proteins of the E3 ligase family. We hypothesized that the MT IVNS1ABP dysregulates the cell cycle through altered protein–protein interactions. Hence, we performed a pull-down assay with an IVNS1ABP antibody, followed by mass spectrometry to identify the potential protein interactors of both wild type (Ctrl) and MT IVNS1ABP (Fig. 5A) using NPCs from the isogenic pairs (Fig. S7A). We identified 36 proteins in Ctrl NPCs and 30 proteins in MT NPCs, with log2foldchange ≥2 compared to IgG control (Fig. S7B). Moreover, 14 proteins were only enriched in Ctrl NPCs with log2foldchange ≥2 compared to MT and nine proteins were enriched in MT NPCs with log2foldchange ≥2 compared to Ctrl (Fig. S7B and Supplementary Data 1). Since cellular senescence and mitotic misregulation could be a consequence of loss-of-function, we focused on the 14 proteins enriched in Ctrl but not MT NPCs. Notably, 10 out of the 14 proteins belonged to the actin/actin-binding protein family (Fig. 5B). The binding between actin and IVNS1ABP was further validated by Co-IP with a pan-actin antibody (Fig. S8A). Apart from ACTB (Actin) itself, most of these proteins were associated with the actomyosin cytoskeleton, contributing to various aspects of actin filament organization, contractility, and dynamics. These include myosin-related proteins, myosin light chain 6 (MYL6), myosin light chain 6B (MYL6B), myosin heavy chain 9 (MYH9), myosin heavy chain 10 (MYH10), and myosin light chain 12B (MYL12B), which regulate non-muscle myosin II activity, which are critical for cell contractility, adhesion and cytokinesis[25]. Additionally, several actin-binding proteins contribute to actin filament stabilization and remodeling. Tropomyosin 1 (TPM1) binds actin filaments to stabilize them and regulate interactions with other actin-binding proteins[26]. Capping actin protein of muscle Z-line beta subunit (CAPZB) forms a heterodimer with CAPZA to cap the barbed ends of actin filaments, thus preventing uncontrolled polymerization[27]. Actin-related protein 2 (ACTR2) is a core component of the actin-related protein 2/3 complex (ARP2/3), which nucleates branched actin networks essential for membrane protrusion and cell motility[28]. Drebrin 1 (DBN1) is involved in stabilizing F-actin structures and plays key roles in cytoskeletal remodeling, particularly in neuronal dendritic spines[29]. These results demonstrate that the IVNS1ABP mutation causes defects in its binding to actin/actin-binding proteins.

The cellular function of actin is regulated by the balance between its monomeric (G-actin) and filamentous (F-actin) forms. To explore the biochemical disparities between WT and MT IVNS1ABP in binding and regulating actin forms, we synthesized WT and MT IVNS1ABP proteins in vitro and conducted an actin co-sedimentation assay. G-actin polymerizes spontaneously, but slowly, under low polymerization conditions in vitro (low salt and low ATP). When incubated with IVNS1ABP, the F-actin pellet was increased in both the WT and MT IVNS1ABP groups, indicating that IVNS1ABP can promote actin polymerization. However, the F-actin amount and binding affinity were significantly reduced in MT IVNS1ABP, compared to WT IVNS1ABP (Fig. 5C and Fig. S8B), suggesting a disrupted capacity of MT proteins in promoting actin polymerization. To determine the binding affinity (K_d) of WT/MT IVNS1ABP with actin, we performed an F-actin pellet assay. WT/MT IVNS1ABP protein at different concentrations (WT: 0.25 to 5 μM; MT: 0.25 to 5 μM) was incubated with F-actin (1 μM) (Fig. S8B, C). The WT IVNS1ABP pelleted F-actin in a dose-dependent manner, while MT IVNS1ABP didn't. Furthermore, the WT IVNS1ABP/actin-binding curve saturated with a K_d of ~1 μM (Fig. S8D). In contrast, the MT IVNS1ABP did not show a significant increase, indicating that the mutation impairs its binding to actin.

The actin polymerization capacity was further measured by the pyrene-actin polymerization assay in the presence of the two forms of IVNS1ABP. Indeed, both forms of IVNS1ABP promoted actin polymerization, although the polymerization rate was lower in the presence of MT IVNS1ABP than the WT (Fig. 5D). The WT IVNS1ABP promoted actin polymerization in a dose-dependent manner with both 1 and 1.5 μM significantly increased the fluorescence intensity compared to actin alone. In contrast, the MT IVNS1ABP only enhanced actin polymerization at 5 μM (Fig. 5D). These findings indicate that the mutation in IVNS1ABP reduces its interaction with F-actin, and thereby dysregulates actin polymerization (Fig. 5E).

Impaired actin polymerization will lead to an imbalance between G-actin and F-actin. By using high-speed centrifugation to separate F- and G-actin, followed by Western blotting, we found a reduced ratio of F- over G-actin in MT and KO NPCs compared to the isogenic controls (Fig. 5F, G). Taken together, our observations indicate that MT IVNS1ABP fails to balance the polymerization and depolymerization of actin.

Dysregulated actin turnover contributes to mitotic defects and DNA damage in MT IVNS1ABP NPCs

The temporal and spatial regulation of actin dynamics is critical for precise cell division. The altered actin dynamics (Fig. 5) and abnormal cell division (Fig. 2) observed in MT IVNS1ABP cells suggest a causal correlation between dysregulated actin dynamics and defective cell division. During mitosis, chromosomal segregation is associated with a

https://doi.org/10.1038/s41467-026-70756-x

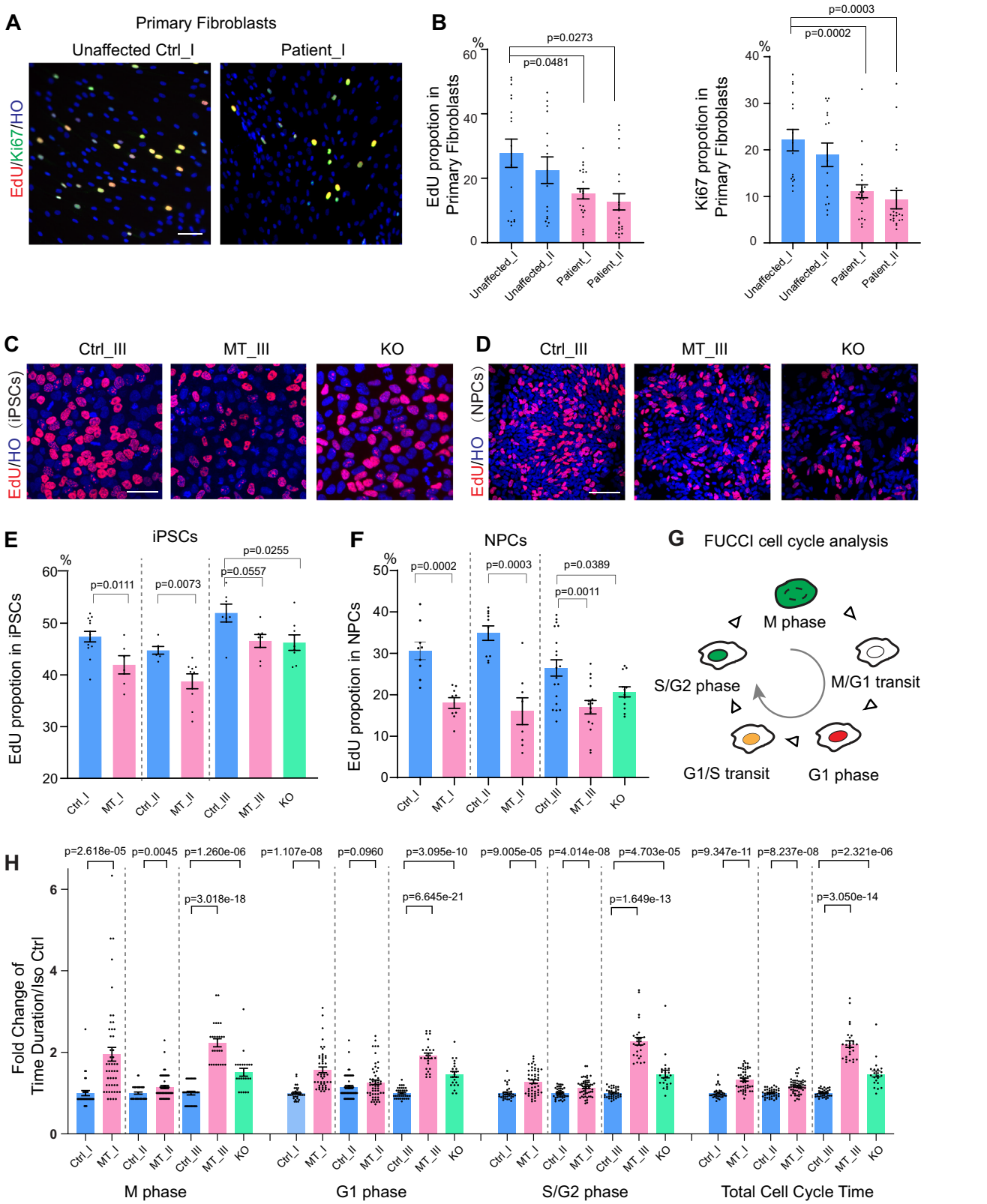

Fig. 3 | Cell cycle arrest mediating mitotic senescence across multiple IVN-S1ABP MT cell lineages. A, B Representative images of EdU/Ki67 staining in primary fibroblasts (**A**) and their quantification (**B**). Total cell numbers were $n = 3144$, 2451, 2570, and 2205 from three independent cultures. Scale bar, 100 µm. **C**–**F** EdU staining in iPSCs (**C**) and NPCs (**D**) from isogenic pair III, quantification in **E** (iPSCs, $n = 9784$, 5286, 2590, 7599, 3600, 4004, and 5302) and **F** (NPCs, $n = 678$, 736, 930, 614, 820, 490, and 360) from three independent cultures. Scale bar, 50 µm. **G** Schematic graph showing time-lapse recording of FUCCI-O labeled iPSCs in different cell cycle stages. **H** Quantification of different cell cycle durations with three isogenic pairs, M phase, G_1 phase, S, and G_2 phase, and total cell cycle duration. Total cell numbers were $n = 32$, 48, 41, 54, 35, 26, and 22 from three independent cultures; each dot represents one cell. Statistical comparisons were performed using unpaired two-tailed *t*-tests for each isogenic cell line pair ($n = 3$ pairs). Each pair was analyzed separately for comparison between the two cell lines within each isogenic background. Data were presented as mean values ± SEM. Source data are provided as a Source Data file.

https://doi.org/10.1038/s41467-026-70756-x

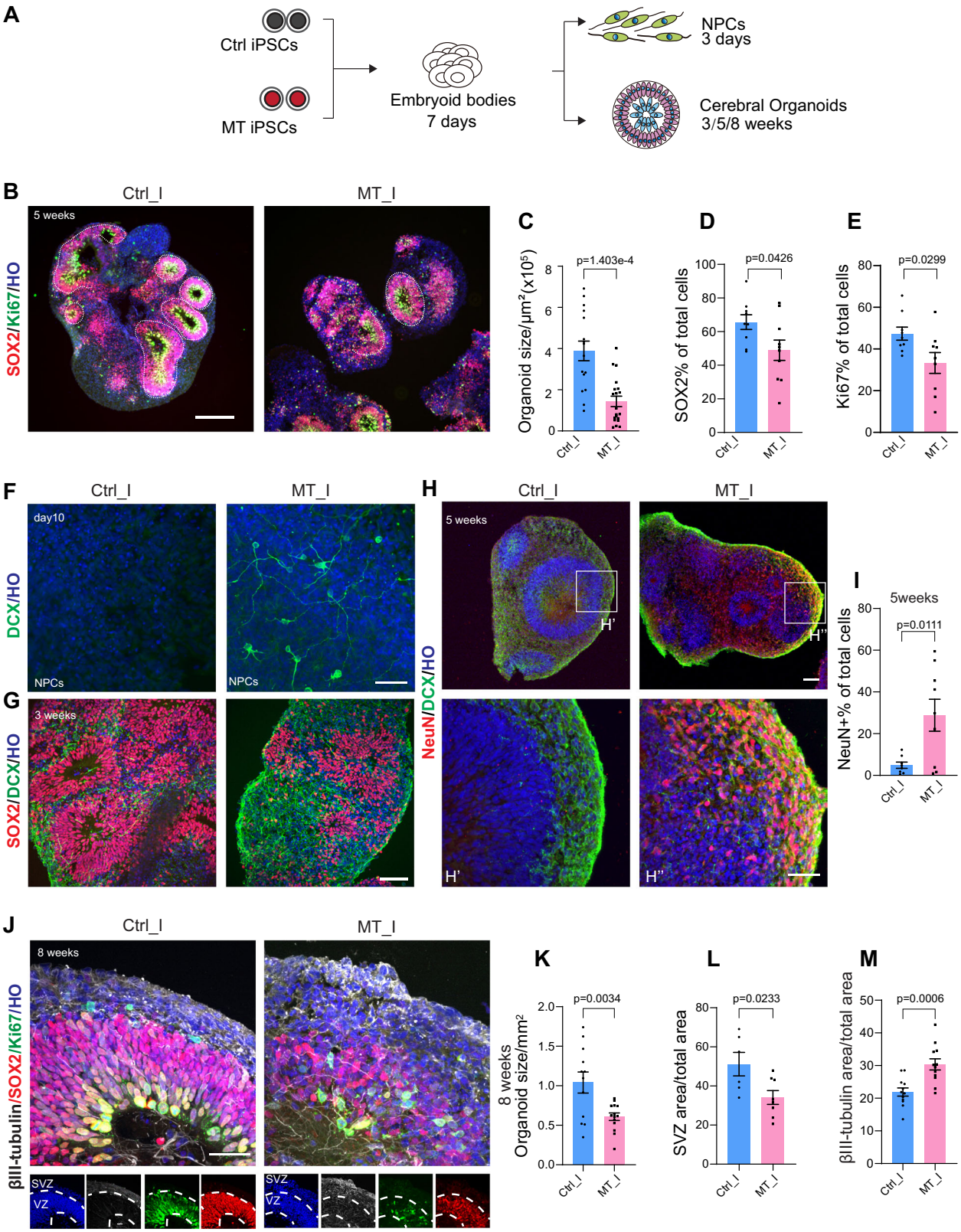

rounding up of cells and the formation of a contractile actomyosin ring. We found that F-actin formed a round and even ring to support cell division in Ctrl NPCs synchronized to the G_2/M phase by nocodazole treatment (Fig. 6A, B). In contrast, F-actin formed an oval and uneven ring in MT NPCs (Fig. 6A, B). Specifically, the actin ring structure was evenly distributed in most of the isogenic cells (89.3%), whereas it was uneven, with actin concentrated in some spots, forming dense aggregates in (24.7%) MT NPCs (Fig. 6B, C). Additionally, the MT NPCs displayed a thinner ring cortex (Fig. 6B, D). The thin and uneven contractile actin filament ring reduces the rigidity of the cortex during cytokinesis[30], contributing to uneven cell division in MT NPCs.

Given that dysregulated actin dynamics impair cytokinesis, regulating actin dynamics and rebalancing the F-actin/G-actin ratio would, at least partially, restore the actin ring structure and hence cell

Fig. 4 | Neural development in 2D and cerebral organoids altered by IVNS1ABP mutation. A Schematic illustration of monolayer (2D) and cerebral organoid (3D) culture systems. **B** Representative images of SOX2 and Ki67 staining in 5-week-old cerebral organoids. Scale bar, 100 µm. **C** Quantification of 5-week-old cerebral organoid size ($n = 16$ and 20, respectively). **D** Quantification of SOX2 percentage in cerebral organoids ($n = 10$ in each group). **E** Quantification of Ki67 percentage in cerebral organoids ($n = 10$ in each group). **F** DCX staining showing newborn neurons in the MT but not the isogenic control group at day 10 of monolayer cultures. Scale bar, 50 µm. The experiment was repeated independently three times with similar results; representative images were shown. **G** Representative images of SOX2 and DCX staining to separate neural progenitors from neurons in 3-week-old organoids. Scale bar, 50 µm. Representative images from three independent experiments with similar results. **H** Representative images of organoids stained for DCX and NeuN. The boxed areas are magnified in H′ for the Ctrl organoids and H″ for the MT organoids. Scale bar, 50 µm. **I** Quantification of NeuN+ cell percentage in 5-week-old cerebral organoids ($n = 8$ and 9, respectively). **J** Representative images of SOX2, Ki67, and βIII-tubulin staining in 8-week-old cerebral organoids, white dashed lines indicate VZ and SVZ-like structure. Scale bar, 50 µm. **K** Quantification of 8-week-old cerebral organoid size ($n = 14$ and 12, respectively). **L** Quantification of the ratio of VZ area to total area at 8 weeks ($n = 6$ and 8, respectively). **M** Quantification of the ratio of βIII-tubulin covered area to total area at 8 weeks ($n = 12$ in each group). Each dot represents one organoid. Statistical comparisons: unpaired two-tailed *t*-tests. Data were presented as mean values ± SEM. Source data are provided as a Source Data file.

division. To test this, we applied a low dose of Jasplakinolide (JPK)[31], an actin polymerization drug, to MT NPCs for 24 h, and found that the F-actin/G-actin ratio was reverted to values similar to those seen in the isogenic control cells (Fig. 6E). Morphologically, the cortical actin ring thickness increased though the aggregates (21.2%, 14/66) did not completely disappear after JPK treatment (Fig. 6F, G). Correspondingly, the rate of normal division, displayed by bipolar spindles with appropriately positioned centrosomes as described in Fig. 2G, rose from 68.63% (35/51) to 77.08% (37/48), suggesting the mitotic defects were mitigated by the enhanced actin polymerization.

We speculated that mitotic defects are likely the main cause of DNA damage (Fig. 1). Indeed, we observed that both MT NPCs and MT organoids showed less SA-β−Gal and γH2AX following treatment with JPK (Fig. 6G–K and Fig. S9). The MT organoids also showed a restored organoid size and SOX2 percentage (Fig. S9), suggesting a potential rescue effect by JPK treatment. Nevertheless, JPK treatment did not alter the expression level of IVNS1ABP (Fig. 6J). Hence, our findings confirm that the mitotic failure and DNA damage seen in IVNS1ABP$^{F253C/F253C}$ cells are mediated by the dysregulated actin dynamics (Fig. 6L).

Discussion

We have revealed the molecular and cellular mechanisms that contribute to the newly identified progeroid neuropathy associated with a recessive loss-of-function mutation in the *IVNS1ABP* gene[13]. Multiple patient cell types, from fibroblasts to iPSCs and NPCs, exhibited prolonged cell cycles, increased expression of p16, heterochromatin loss, and increased DNA damage. These cellular senescence phenotypes were eliminated when the mutation was corrected, or mimicked when the mutation was introduced into unaffected cells. Taken together, they resembled those of KO, suggesting a potential loss- of-function of IVNS1ABP in the disease pathogenesis. Furthermore, proteomics and transcriptomics studies pointed to alterations in actin and its associated proteins in cellular senescence. Indeed, MT IVNS1ABP showed decreased binding affinity to actin, leading to dysregulated actin dynamics during cytokinesis, and subsequently, premature neural differentiation and cellular senescence. Strikingly, restoration of the F- and G-actin balance, even in the presence of IVNS1ABP mutation, mitigated cellular senescence. Taken together, our study has identified dysregulated actin dynamics caused by MT IVNS1ABP as a mediator of premature aging in this newly identified progeria-like syndrome.

The biological function of IVNS1ABP

IVNS1ABP was first identified as a novel human protein termed NS1-BP, in the search for interacting proteins of influenza A virus NS1 protein, through a yeast interaction trap system[14]. The murine homolog was named as Nd1 (*ncx* downstream gene 1), as it was isolated from an *Ncx*-deficient mice. Nd1 encodes two isoforms−a long (Nd1-L) and a short (Nd1-S) form−with the former being the actin-binding isoform[18]. In humans, it has only one reported form under normal conditions, equivalent to Nd1-L. Notably, *Nd1*-deficent mice showed no cardiac or gross anatomical abnormality[32], although our human cellular IVNS1ABP KO model showed severe deficits in the CNS, highlighting the potentially unique functions of human IVNS1ABP.

As a Kelch protein, IVNS1ABP, when mutated, may contribute to neuropathy and aging via multiple pathways. The highly conserved BTB/BACK domain suggests its recruitment to E3 ubiquitin ligase complex, indicating that IVNS1ABP plays a role in protein homeostasis. We indeed observed protein aggregations and enlarged lysosomes in multiple IVNS1ABP-mutated cell types, including NPCs and neurons[13]. Mutations in its paralog KLHL16 result in similar outcomes, where patients present with Giant axonal neuropathy-1 (GAN1) due to impaired proteostasis and accumulation of cytoskeleton proteins in axons[33]. Unlike many other Kelch proteins, IVNS1ABP does not bind Cullin3, but may regulate ubiquitination through interaction with other KLHL family members such as KLHL20[16]. KLHL proteins belong to a subfamily of Kelch-repeat proteins, which are known for their role in actin cytoskeleton organization in *Drosophila*[34]. Other KLHL proteins, such as KLHL1, Mayven (KLHL2) and IPP (KLHL27), have been shown to bind actin directly[35–37]. Our proteomics analysis and Co-IP further validated the interactions of IVNS1ABP with actin and actin-binding proteins, suggesting that IVNS1ABP may regulate cellular activity via actin.

Mutant IVNS1ABP dysregulates actin polymerization and mitosis

Actin, a central player in basic cell function, is highly conserved. Notably, IVNS1ABP mutation impairs its ability to bind actin, leading to reduced F-actin/G-actin ratio and disorganization of actin filaments, such as their aggregation, during cell division. Furthermore, alterations in the F-actin/G-actin ratio in the mutants suggest a role of IVNS1ABP in actin polymerization/depolymerization, and consistent with this, our polymerization assay revealed a reduced polymerization capacity in IVNS1ABP MT cells.

A precise regulation of actin polymerization and depolymerization is crucial for many biological processes, such as cytokinesis. At the metaphase, when the cell prepares to divide, actin polymerizes, and the actin filaments organize into a cortical ring that serves as an anchor for microtubules to pull the chromosomes to the opposite directions equally[38]. However, our studies showed that IVNS1ABP mutations altered the dynamics of actin polymerization, resulting in the formation of a thin and uneven cortical ring. We propose that this could be the basis of several defects during cytokinesis, including multipolar division, micronuclei, lagging chromosomes, monopolar spindle and misaligned spindles. These mitotic catastrophes result in cell death, evidenced by the disappearance of cells shortly following division. Severe mitotic failure and prolonged cell cycles create genome instability and DNA damage, contributing to senescence.

IVNS1ABP mutation leads to mitotic senescence

Mitotic senescence is a common mechanism underlying progeroid syndromes. Similar to the most common progeroid syndrome, HGPS, our patient cells exhibit retarded cell growth, readily characterized by

https://doi.org/10.1038/s41467-026-70756-x

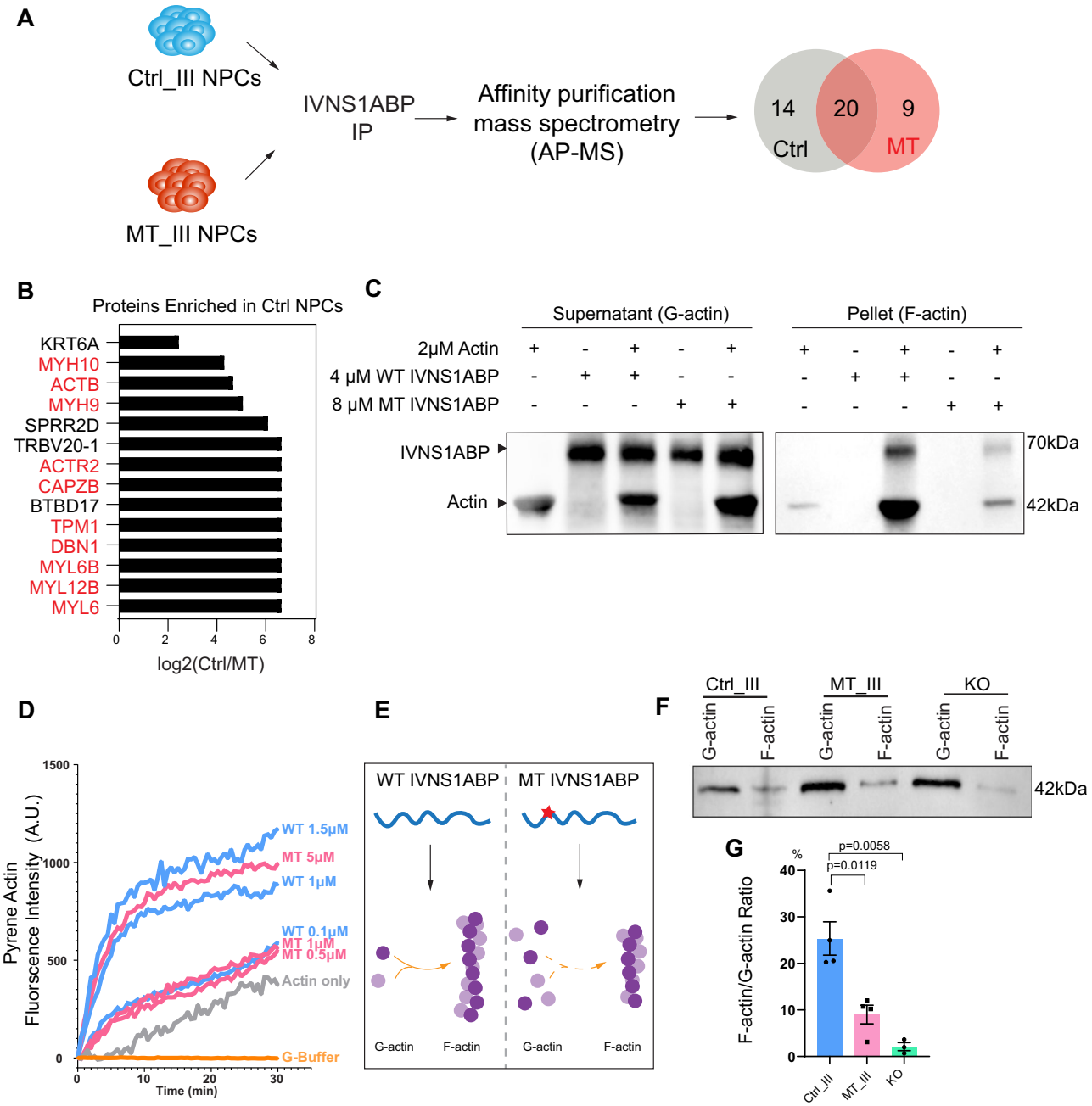

Fig. 5 | Actin dynamics altered by MT IVNS1ABP. A Flow chart showing affinity purification mass spectrometry (AP-MS) analysis to identify proteins interacting with WT/MT IVNS1ABP. $n = 3$ in each group (WT, MT, IgG). **B** Protein interactors enriched with WT IVNS1ABP, actin/actin-binding proteins labeled in red. **C** Actin co-sedimentation assay with WT/MT IVNS1ABP presented as immunoblots showing ACTIN and IVNS1ABP expression. Left blot showing G-actin and IVNS1ABP, right blot showing F-actin spinning down together with IVNS1ABP. Representative of three independent experiments with similar results. **D** Pyrene-actin fluorescence assay showing actin polymerization with WT/MT IVNS1ABP (WT IVNS1ABP protein concentration: 0.1 to 1.5 μM; MT IVNS1ABP protein concentration: 0.5 to 5 μM. Pyrene-actin concentration is ~10 μM). Representative of three independent experiments with similar results. **E** Cartoon showing potential interaction between WT/MT IVNS1ABP and G-actin and F-actin; Created in BioRender. Y, F. (2026) https://BioRender.com/5mq77fn. **F** Immunoblot and quantification (**G**) of F-actin/G-actin ratio in iPSC-derived NPCs in isogenic pair III. Ctrl and MT were collected from four independent cultures, and KO were collected from three independent cultures. Data were presented as mean values ± SEM and performed by unpaired two-tailed *t*-tests. Source data are provided as a Source Data file.

the slow expansion of the dermal fibroblasts, smaller colonies of iPSCs, and reduced incorporation of EdU in NPCs. At the molecular level, MT NPCs exhibit upregulated CDK inhibitor CDKN2A/p16, increased DNA damage, loss of chromatin components and increased expression of cellular senescence genes. In contrast to HGPS, where CNS senescence is absent, patients with the IVNS1ABP mutation display senescence in the CNS cells too. This is likely due to the fact that the Lamin A mutation in HGPS does not affect Lamin C-expressing CNS cells[39]. In contrast, the IVNS1ABP mutation in this newly identified disease negatively regulates actin, which is universally expressed in all cell types, including neural cells. This could explain the reporting of neurological defects, in addition to progeria symptoms, in patients with the IVNS1ABP mutation.

Furthermore, dysregulated actin filament organization during cytokinesis results in cell cycle arrest, which could potentially lead to precocious cell cycle exit and premature differentiation of neural progenitors. Indeed, the postmitotic neurons appeared substantially earlier in the mutant cells in both our 2D cultures and 3D organoids.

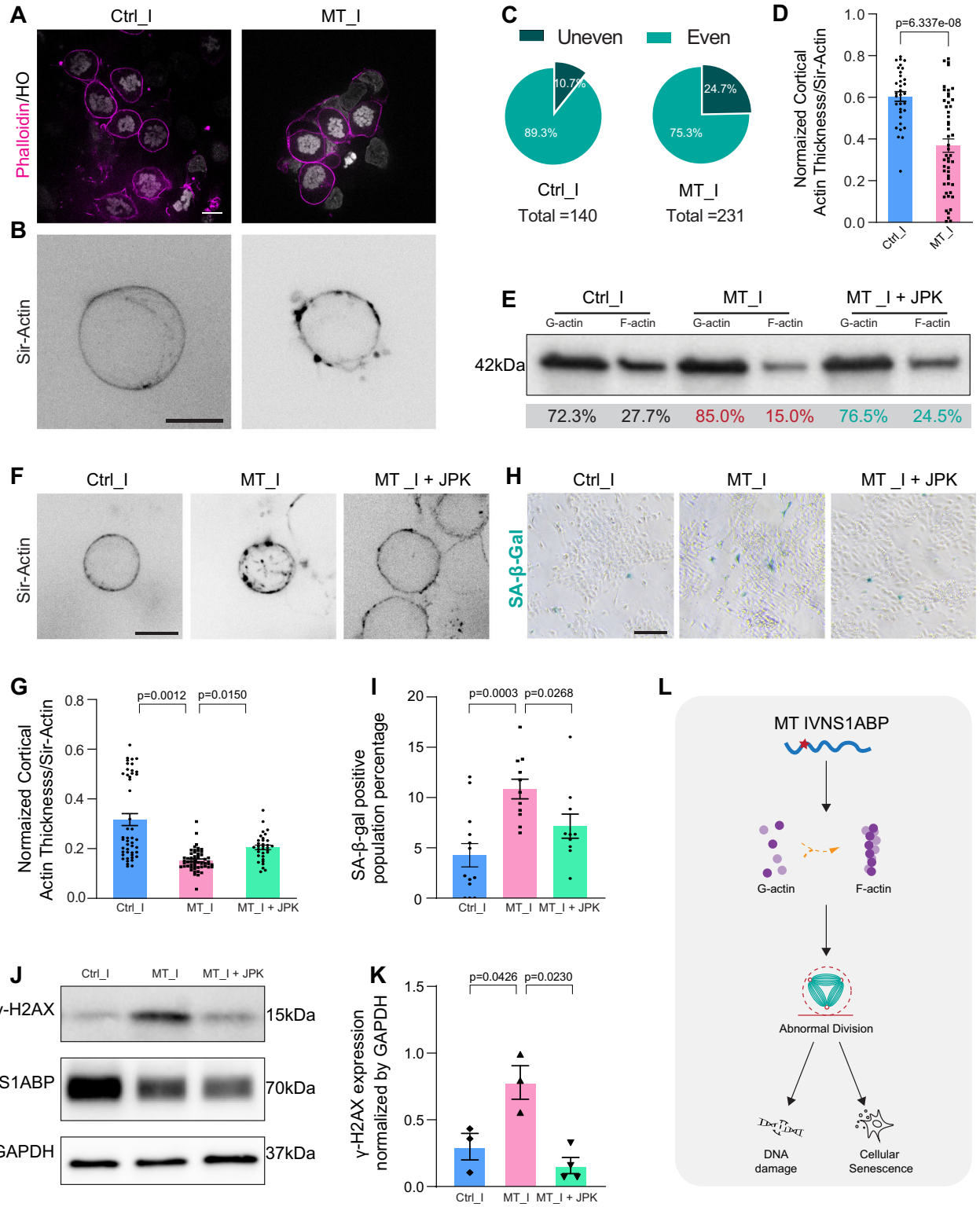

The early cell cycle exit and premature differentiation result in fewer neurons and axons, reflected in the thinner corpus callosum and cerebellar vermis exhibited by the patients[13]. Actin dynamics is crucial for synaptic plasticity in neurons; actin dysregulation is highly associated with age-related cognitive decline[40,41], potentially explaining the cognitive impairment in our patients. Dysregulated actin dynamics impair axonal integrity, in addition to impaired proteostasis[13], leading to neuropathy. Further studies are needed to examine in detail the impact of MT IVNS1ABP on neural development, maintenance, and plasticity.

In summary, we identified a new premature aging syndrome with neurological and cognitive deficits caused by a homozygous variant in the *IVNS1ABP* gene. MT IVNS1ABP, similar to the gene KO, impairs its ability to bind actin and actin-associated proteins, and thus, dysregulates actin polymerization. Dysregulated actin polymerization disrupts precise cytokinesis in mitotic cells, leading to cell cycle arrest and cellular senescence. Precocious cell cycle exit coupling with premature neural differentiation, leads to fewer neurons and axons as well as impaired synaptic function, and hence complex syndromes, such as neurological and cognitive deficits.

Fig. 6 | Structure and polymerization of actin are altered by MT IVNS1ABP. **A** Representative images of actin ring structure during mitosis in NPCs of the MT and isogenic control groups labeled by Phalloidin. Scale bar, 10 μm. **B** Super-resolution images of live actin ring structure during mitosis in NPCs of the MT and isogenic control groups labeled by Sir-Actin. Scale bar, 10 μm. **C** Quantification of uneven actin ring structure during mitosis from three independent cultures. Actin ring containing aggregates larger than 1 ⌈m in diameter, as identified by ComDet in ImageJ, was classified as uneven. **D** Quantification of normalized actin cortex ring thickness from three independent cultures by a self-written MATLAB script ($n = 33$ and 50, respectively), each dot represents the actin ring thickness measured from one mitotic cell. **E** Representative immunoblot of F-actin/G-actin ratio in Ctrl, MT, and JPK-treated MT NPCs from three independent cultures. **F** Super-resolution images of live actin ring structure during mitosis in NPCs of the MT, the isogenic control groups, and JPK-treated MT groups labeled by Sir-Actin. Scale bar, 10 μm. **G** Quantification of normalized actin cortex ring thickness with JPK treatment from three independent cultures ($n = 25$, 31, and 27, respectively). **H** Representative images of β-Galactosidase staining in the Ctrl, MT, and JPK-treated MT NPCs. Quantification in (**I**) (cell numbers $n = 1586$, 1255, and 2094 from three independent cultures). Scale bar, 50 μm. **J**, **K**Immunoblot and quantification of γH2AX (**K**), IVNS1ABP and GAPDH in Ctrl, MT, and JPK-treated MT NPCs. Data were collected from three independent cultures. **L** Schemic graph showing that MT IVNS1ABP results in abnormal division through dysregulated actin dynamics. Data were presented as mean values ± SEM and performed by unpaired two-tailed Student's *t*-tests. Source data are provided as a Source Data file.

Limitations of the study. Due to the lack of a model system for the new disease, we used the iPSC model. While we aimed to rigorously control the system by using multiple pairs of isogenic iPSCs and by both correcting and knocking in mutations, we noticed some disparities among the iPSC lines. The isogenic pair II, derived by introducing the mutant IVNS1ABP into the unaffected sibling, showed relatively mild phenotypes compared to the two other isogenic pairs derived from patients. This could be a consequence of individual variations. Alternatively, the disease iPSCs potentially carry additional changes due to the genomic instability of the mutant cells. Thus, additional model systems, especially in vivo models such as the zebrafish[13] or mammalian models, will help further elucidate the disease process. The present study focuses on actin dysregulation by the mutant IVNS1ABP; it is likely that other pathways, such as proteostasis[13], are involved.

Methods

Generation of iPSCs

This study was conducted in accordance with all relevant ethical regulations. Generation/use of patient-derived cell lines were approved by the National University of Singapore Institutional Review Board (NUS-IRB) under protocol # LH-18-027R. Written informed consent was obtained from all participants.

iPSCs were derived from primary cutaneous fibroblasts[13]. Fibroblasts of two patients and one healthy control were reprogrammed using the CytoTune™-iPS 2.0 Sendai Reprogramming Kit (Thermo Fisher Scientific, A16517) in accordance with the manufacturer's instructions. Briefly, fibroblasts were transduced with Yamanaka's four transcription factors, and after 7 days, were plated onto Matrigel Basement Membrane Matrix (Corning, 354234) in mTeSR1 medium (STEMCELL Technologies, 85850). iPSC colonies were picked between days 17–28 and maintained on Matrigel and mTeSR1 for expansion.

Gene editing of iPSCs by CRISPR/Cas9

Human iPSCs were maintained under feeder-free conditions, and treated with Rho Kinase (ROCK) inhibitor 24 h before electroporation. A guide RNA was designed using the CRISPR design tool (http://chopchop.cbu.uib.no/); the ~75nt donor single-stranded oligodeoxynucleotides (ssODNs) were designed with homologous genomic flanking sequence centered around the CRISPR/Cas9 cleavage site containing point mutation[42]. The iPSC cultures (1×10^6) were dissociated into single cells by EDTA for 5 min, and then were mixed with reagents (4 μg Cas9 nuclease, 150 pmole sgRNA, and 2 nmole ssODN) (IDT Technologies). The cell mixture was electroporated using the Neon transfection System (Invitrogen) with the following parameters: Voltage 1200 V, Width 30 ms, and 1 Pulse. After electroporation, the cells were reseeded on a vitronectin-coated six-well plate in Essential 8 medium, with the addition of ROCK inhibitor for the first 24 h. Stable colonies were selected 2–3 days after seeding. Positive colonies were confirmed with Sanger Sequencing, following which they were expanded and stored. The top five predicted off-target sites were amplified and Sanger Sequenced, and then compared with the unedited cell line. Karyotype tests were performed by the Cytogenetics Lab at Singapore General Hospital. Pluripotency of the iPSCs were confirmed by TRA-1-60 and NANOG staining. The guide RNA sequence, ssODN template sequence and off-target information are included in Supplementary Data 2.

Culturing of human iPSCs and NPCs

Human iPSCs (Passage 10–40) were maintained on vitronectin-coated plates (Life Technologies) with Essential 8 medium, which was changed daily. Cells were passaged every 5 days through ethylenediaminetetraacetic acid (EDTA) (Lonza) digestion. Neuron differentiation was carried out according to our previously established protocol[20]. Briefly, hPSCs were detached by dispase (Life Technologies) to form embryoid bodies (EBs) and then cultured in neural induction medium (DEMEMF12 medium supplemented with 100x N2 and 100x NEAA). After floating culture for 7 days, EBs were attached, and rosette structures could be observed at days 10–16. At day 16, rosette colonies were detached manually with a 1 ml pipette. Non-neural epithelial clones were removed at this stage. Neural progenitors were used for analysis at day 10 or day 20. To culture organoids, EBs were continuously cultured in neural induction medium (NIM) for 3 weeks or longer.

Immunochemistry

Cells cultured on coverslips or organoid samples were fixed in cold fresh 4% paraformaldehyde for 30 min and rinsed three times with phosphate-buffered saline. Organoid samples were further dehydrated in PBS solution containing 30% sucrose for 1 day and sectioned at a 30-μm thickness. Cells or organoid sections were treated with 0.2% Triton X-100 for 10 min and blocked in 10% donkey serum for 1 h. Cells were incubated at 4 °C overnight in the primary antibody diluted with 0.1% triton and 5% donkey serum. On the second day, cells were incubated in secondary antibody diluted in 5% donkey serum for 30 min at room temperature. Coverslips were mounted for fluorescent imaging. The primary and secondary antibodies are listed in Supplementary Data 3.

EdU cell proliferation assay

Cell proliferation was assessed by EdU incorporation assay using Click-iT Plus EdU Alexa Fluor 555 imaging kit (Thermo Fisher). In brief, iPSCs were passaged to 24-well Matrigel precoated glass coverslips, around 5000 cells/coverslip. After 48 h, cells were incubated with 10 μM EdU for 30 min and then fixed. For NPCs, NPCs differentiated from iPSCs for 14 days were seeded on the coverslip, around 20,000 cells/coverslip. The next day, cells were incubated with 10 μM EdU for 30 min. For primary fibroblasts, cells were passaged to 24-well poly-L-ornithine-precoated glass coverslips, around 5000 cells/coverslip. After 24 h, cells were incubated with 10 μM EdU for 18 h and then fixed, permeabilized, and stained before proceeding to imaging.

Western blot

Cells were washed with cold PBS, scratched and lysed on ice using RIPA lysis buffer (Thermo Fisher) together with protease inhibitor, phosphatase inhibitor, phenylmethylsulfonyl fluoride and dithiothreitol.

Total protein concentration was measured by the BCA protein assay. 4X Laemmli sample buffer was added to the protein lysate and boiled at 100 °C for 5 min. Protein samples were loaded on 4–20% Mini-Protein SFX precast gel (Bio-Rad), and then transferred to polyvinylidene difluoride membranes, blocked with 5% non- fat dry milk TBST, and then incubated with primary antibodies overnight at 4 °C. Signals were visualized using horseradish peroxidase-conjugated secondary antibodies, the ECL system and captured with the ChemiDoc system. Antibodies are included in Supplementary Data 3.

FUCCI cell cycle analysis

The FUCCI system was introduced into cells through lentiviral transfection. For viral particle generation, HEK293T cells were transfected with second-generation lentivirus plasmids pCMV-VSV-G (Addgene #8454), psPAX2 (Addgene #12260), and pBOB-EF1-FastFUCCI-Puro (Addgene #86849). Viral particles were collected 48 h post transfection and purified by ultracentrifugation. IPSCs were transfected with FUCCI virus and screened by puromycin for 2 days. FUCCI-expressing cells were then expanded and passaged for subsequent live cell imaging experiments. iPSCs positively expressing FUCCI were seeded on confocal dishes and recorded 48 h after passaging. To minimize the potential toxic impact of the cell cycle synchronization molecules, we used time-lapse recording and followed the cells throughout the cycle.

Measurement of G-actin/F-actin ratio

G-actin/F-actin ratio was determined by immunoblotting of a specific actin antibody using a G-actin/F-actin assay kit (Cytoskeleton). Briefly, Ctrl/MT NPCs were lysed in a detergent-based lysis buffer, which stabilizes and maintains the G-and F-forms of cellular actin. The two forms of actin differ in that F-actin is insoluble, whereas G-actin is soluble in the lysis buffer. The G-actin and F-actin fractions were separated using an ultracentrifuge (TLA100 rotor; Beckman Coulter) at 100,000×*g* for 1 h at 37 °C. G-actin was persevered in the supernatant, while F-actin in the pellet was depolymerized to G-actin in the same volume of depolymerization buffer. Equal amounts of supernatant (G-actin) and pellet (F-actin) fractions were mixed with 5X SDS sample buffer and processed for western blotting.

RNA-seq analysis

Human iPSCs (Ctrl/MT/KO) and NPCs (Ctrl/MT/KO) from isogenic pair III were collected for total RNA extraction, and each sample was processed in triplicate. Whole transcriptome RNA-seq was performed by Novogene Singapore Pte. Ltd. with 40 million 150 bp pair-end reads per library. The quality of the sequencing library was evaluated with FastQC. Following this, Salmon was used to align sequencing reads to the human transcriptome (hg38)[43], and Deseq2 was used for differential gene expression analysis. Differentially-expressed genes between MT and WT samples were identified based on p value ≤0.05 and fold-change ≥2[44]. Weighted gene co-expression network analysis (WGCNA) was performed with the WGCNA package in R[45]. Co-expression gene modules between MT and WT were constructed using Blockwise, with default settings and a power threshold of 9. Each resulting module was subsequently subjected to functional analysis using the Modules function. The genomic background for this analysis encompassed all genes expressed in the current dataset. Each module was enriched for GO biological processes using ClusterProfiler[46]. Only gene sets that passed a multiple test adjustment using the Benjamini–Hochberg procedure (adj. $p \leq 0.05$) were deemed significantly-enriched in a biological process.

Co-immunoprecipitation

Approximately 20 million Ctrl/MT NPCs were lysed for 30 min through vortexing and pipetting up and down, using 500 µL Pierce™ IP buffer (Thermo Fisher) supplemented with protease inhibitors. About 25 µl Protein G beads (Pierce™ Protein A/G Magnetic Beads, Thermo Fisher) were prewashed three times with Tris-buffered saline containing 0.05% Tween-20, and subsequently collected with a magnetic stand. The beads were further incubated with either IVNS1ABP antibody (Anti-Ms, Santa Cruz) or IgG (Anti-Ms, Millipore) antibody for 1 h with gentle rotation at room temperature, followed by an overnight incubation with cell lysates at 4 °C. The next day, the supernatant was saved for analysis, and the beads were washed thrice with Tris-buffered saline containing 0.05% Tween-20, and once with water. After washing, the supernatant containing the antigen was separated from the beads magnetically by elution. Eluted bead-bound proteins were further processed with neutralizing buffer (1 M Tris) before electrophoresis in SDS-PAGE. The total protein lysate (input) and the IP fractions (output) were analysed by immunoblotting using the IVNS1ABP antibody (Anti-Rb, Novus).

Affinity purification mass spectrometry (AP-MS) analysis

The co-IP fractions were prepared from independent biological replicates ($n = 3$ independent IPs per group: WT, MT, and IgG control; total = 9 samples). Proteins were extracted with lysis buffer and universal nuclease (EasyPep™ Mini MS Sample Prep Kit, Thermo Fisher). Protein quantitation was done using the DC Protein Assay (Bio-Rad Laboratories Inc., California, USA). The protein solutions were then reduced, alkylated, digested and cleaned up according to the manufacturer's instructions (EasyPep™ Mini MS Sample Prep Kit, Thermo Fisher). Peptides were reconstituted in 2% Acetonitrile and 0.1% formic acid in water, and peptide concentration was determined by Thermo Scientific Pierce™ Quantitative Fluorescent Peptide Assay.

The reconstituted samples were then analyzed on an EASY-nLC 1200 system coupled to an Orbitrap Exploris™ 480 mass spectrometer (Thermo Fisher). The Easy-nLC system was equipped with a 100 C18, 3 µm, 75 µm × 2 cm in-line trap column of PepMap and a C18, 2 µm, 25 cm × 75 µm Easy-spray Pepmap RSLC column. The EASY-nLC was operated at a flow rate of 300 nL/min. Mobile phase A consisted of 0.1% formic acid in LC-MS grade water, and mobile phase B was made up of 0.1% formic acid and 80% acetonitrile in LC-MS grade water. The gradient comprised of a 29 min step gradient from 5 to 60% mobile phase B and 1 min from 60 to 98% solvent B. The Orbitrap ExplorisTM 480 mass spectrometer was operated in data-independent and positive ionization mode. LC-MS/MS analysis was performed as described below: MS1 spectra were recorded at a resolution of 60k with MaxIT mode set to auto. The scan range was 350 to 1600 m/z for full scan. The automatic gain control (AGC) target was set to custom with a normalized AGC target at 300%. Peptides were then selected for ddMS2 using HCD Collision energy at 28% with a fixed collision energy mode, and the fragments were detected in the Orbitrap at a resolution of 15k with auto MaxIT. The isolation window was set to custom with m/z set to 1.6. The first mass was set at m/z 120. The AGC target was set to custom with normalized AGC target set to 75%. The resulting MS/MS data were processed using Proteome Discoverer version 2.5 (Thermo Fisher). Data were provided in Supplementary Data 4.

β-Galactosidase staining

Senescence-associated β-galactosidase (SA-β-Gal) activity was assessed using a commercial staining kit (Cell Signaling) according to the manufacturer's instructions. NPCs were seeded on a six-well plate and washed with PBS, fixed with 0.5% glutaraldehyde for 10–15 min at room temperature, and incubated overnight at 37 °C (without CO_2) in staining solution containing X-gal and then proceeded to image.

Protein generation and actin co-sedimentation assay

WT/MT IVNS1ABP cDNA fragments were obtained by PCR amplification of the cell extracts, and subsequently inserted into pTNT™ Vector (Promega) following the manufacturer's instructions. The WT/MT IVNS1ABP constructs were then processed using the TNT® Quick Coupled Transcription/Translation Systems (Promega) to express WT/

MT IVNS1ABP proteins. The expression of these proteins was further verified by immunoblotting with an IVNS1ABP-specific antibody.

Actin co-sedimentation assay was performed using the actin-binding spin-down kit (Cytoskeleon). Briefly, G-actin protein solution was incubated with WT/MT IVNS1ABP protein at RT for 30 min in the polymerization buffer (1 mM ATP, 2 mM $MgCl_2$, 50 mM KCl, 0.2 mM $CaCl_2$, ~5 mM Tris-HCl, pH 7.5–8.0) and sedimented at 150,000×*g* (TLA100 rotor; Beckman Coulter) for 1.5 h at RT. The G-actin and F-actin fractions were then separated and immunoblotted with actin and IVNS1ABP antibody.

F-actin pellet assay

To assess F-actin binding, we performed a high-speed co-sedimentation assay following a previously published protocol[47]. Briefly, purified WT/MT IVNS1ABP proteins were incubated with pre-polymerized F-actin at room temperature for 30 min in reaction buffer (20 mM imidazole, pH 7.0, 0.15 M NaCl, 0.2 mM MgCl2, 0.5 mM ATP, and 1 mM EGTA). Samples were then centrifuged at 100,000×*g* for 20 min at 4 °C to pellet the actin filaments and any associated proteins. The supernatant and pellet fractions were separated, mixed with SDS sample buffer, and analyzed by SDS-PAGE. Proteins that bound to F-actin were detected in the pellet fraction. Control reactions lacking F-actin were included to account for nonspecific sedimentation. Quantitative analysis was performed to assess binding efficiency.

Pyrene-actin polymerization assay

Actin polymerization rates were measured using the commercial Actin Polymerization Biochem Kit (Cytoskeleton). The fluorescence signal of pyrene-monomeric actin is enhanced seven to ten times during its assembly into filaments, making it an ideal tool for tracking actin polymerization[48]. Pyrene G-actin was freshly prepared by depolymerizing actin oligomers and removing residual filaments via ultracentrifugation. In a 96-well black plate, pyrene G-actin (10 µM) was mixed with buffer (5 mM Tris-HCl, pH 8.0, and 0.2 mM $CaCl_2$) and varying concentrations of WT or MT IVNS1ABP (ranging from 0.1 to 5 µM). After a 3-min preincubation in a fluorescence spectrophotometer (Tecan Infinite M200), polymerization was initiated by adding the supplied polymerization buffer (1 mM ATP, 2 mM $MgCl_2$, and 50 mM KCl). Fluorescence was measured every 30 s for 1 h (excitation: 365 nm, emission: 385 nm).

Drug treatment

Jasplakinolide (Thermo Fisher) stock solution was prepared at 1 mM in DMSO. For experiments, it was first diluted to 1 µM in culture medium, and then further diluted 100-fold into the final medium to achieve a working concentration of 10 nM. Equivalent DMSO concentrations (0.001%) without JPK were included in all JPK-related experiments controls (Ctrl + Vehicle and MT + Vehicle), to account for any effects of the solvent itself.

NPCs were treated with 100 nM Nocodazole (Invitrogen) for 16 h to synchronize to G_2/M phase[49], and then washed twice with PBS. Following treatment, cells were either immediately fixed for downstream analysis or washed out into fresh medium to monitor progression through mitosis.

Microscopy/live cell Imaging

Images were captured using a Nikon Ti2 inverted microscope equipped with a Yokogawa spinning disk confocal, GATACA super-resolution systems (SIM) and a sCMOS camera (Prime 95B). For live imaging experiments, images were acquired at 37 °C with 5% CO^2 using an on-stage incubator and CO_2 mixer (LCI), and cells were imaged in multi channels by sequential laser excitations at 488, 561, or 642 nm through a quad-bandpass dichroic mirror (Semrock) and single band emitters (Semrock). For FUCCI recording, movies were acquired on a single z plane with a speed of 5 min/frame or 10 min/frame, and exposure times in the 100–300 ms range. The actin ring structure was captured with SIM microscopy. Immunostaining images were taken with z-stack acquisition with 0.5 or 1 µm step-size and processed with maximum projection images of multiple z-stacks.

Quantification and statistical analysis

Data was analysed by GraphPad Prism version 8. All bar graphs are presented as mean values ± SEM. Replicate sizes and error bars are indicated in the figure legends. Statistical comparisons were performed using unpaired two-tailed Student's *t*-tests for each isogenic cell line pair ($n = 3$ pairs). Each pair was analyzed separately for comparison between the two cell lines within each isogenic background. $^*p \le 0.05$; $^{**}p \le 0.01$; $^{***}p \le 0.001$.

Reporting summary

Further information on research design is available in the Nature Portfolio Reporting Summary linked to this article.

Data availability

RNA-sequencing data were deposited to Gene Expression Omnibus (GEO) under GSE270946, and raw proteomics data were deposited to ProteomeXchange (Identifier: PXD053645). These are publicly available with no restrictions. All data supporting the findings of this study are available within the paper and its Supplementary Information. Source data are provided with this paper.

References

1. López-Otín, C., Blasco, M. A., Partridge, L., Serrano, M. & Kroemer, G. Hallmarks of aging: an expanding universe. *Cell* **186**, 243–278 (2023).
2. Gorgoulis, V. et al. Cellular senescence: defining a path forward. *Cell* **179**, 813–827 (2019).
3. Ly, D. H., Lockhart, D. J., Lerner, R. A. & Schultz, P. G. Mitotic misregulation and human aging. *Science* **287**, 2486–2492 (2000).
4. Nagaoka, S. I., Hassold, T. J. & Hunt, P. A. Human aneuploidy: mechanisms and new insights into an age-old problem. *Nat. Rev. Genet.* **13**, 493–504 (2012).
5. Macedo, J. C. et al. FoxM1 repression during human aging leads to mitotic decline and aneuploidy-driven full senescence. *Nat. Commun.* **9**, 2834 (2018).
6. Sieben, C. J. et al. BubR1 allelic effects drive phenotypic heterogeneity in mosaic-variegated aneuploidy progeria syndrome. *J. Clin. Investig.* **130**, 171–188 (2020).
7. Baker, D. J. et al. BubR1 insufficiency causes early onset of aging-associated phenotypes and infertility in mice. *Nat. Genet.* **36**, 744–749 (2004).
8. De Sandre-Giovannoli, A. et al. Lamin A truncation in Hutchinson-Gilford progeria. *Science* **300**, 2055 (2003).
9. Dechat, T. et al. Alterations in mitosis and cell cycle progression caused by a mutant lamin A known to accelerate human aging. *Proc. Natl Acad. Sci. USA* **104**, 4955–4960 (2007).
10. Scaffidi, P. & Misteli, T. Lamin A-dependent nuclear defects in human aging. *Science* **312**, 1059–1063 (2006).
11. Nissan, X. et al. Unique preservation of neural cells in Hutchinson-Gilford progeria syndrome is due to the expression of the neural-specific miR-9 microRNA. *Cell Rep.* **2**, 1–9 (2012).
12. Baek, J.-H. et al. Expression of progerin in aging mouse brains reveals structural nuclear abnormalities without detectible significant alterations in gene expression, hippocampal stem cells or behavior. *Hum. Mol. Genet.* **24**, 1305–1321 (2014).
13. Bonnard, C. et al. Loss of IVNS1ABP, a gigaxonin paralogue, leads to a progeroid neuropathy due to impaired proteostasis. Preprint at *medRxiv* https://doi.org/10.1101/2024.10.23.24315364 (2024).
14. Wolff, T., O'Neill, R. E. & Palese, P. NS1-binding protein (NS1-BP): a novel human protein that interacts with the influenza A virus

nonstructural NS1 protein is relocalized in the nuclei of infected cells. *J. Virol*. **72**, 7170–7180 (1998).
15. Zhang, K. et al. Structural-functional interactions of NS1-BP protein with the splicing and mRNA export machineries for viral and host gene expression. *Proc. Natl. Acad. Sci. USA* **115**, E12218–E12227 (2018).
16. Chen, H. Y. et al. KLHL39 suppresses colon cancer metastasis by blocking KLHL20-mediated PML and DAPK ubiquitination. *Oncogene* **34**, 5141–5151 (2015).
17. Robinson, D. N. & Cooley, L. *Drosophila* kelch is an oligomeric ring canal actin organizer. *J. Cell Biol*. **138**, 799–810 (1997).
18. Sasagawa, K. et al. Identification of Nd1, a novel murine kelch family protein, involved in stabilization of actin filaments. *J. Biol. Chem*. **277**, 44140–44146 (2002).
19. Thaventhiran, J. E. D. et al. Whole-genome sequencing of a sporadic primary immunodeficiency cohort. *Nature* **583**, 90–95 (2020).
20. Li, X.-J. et al. Coordination of sonic hedgehog and Wnt signaling determines ventral and dorsal telencephalic neuron types from human embryonic stem cells. *Development* **136**, 4055–4063 (2009).
21. d'Adda di Fagagna, F. Living on a break: cellular senescence as a DNA-damage response. *Nat. Rev. Cancer* **8**, 512–522 (2008).
22. Kuilman, T., Michaloglou, C., Mooi, W. J. & Peeper, D. S. The essence of senescence. *Genes Dev*. **24**, 2463–2479 (2010).
23. Sakaue-Sawano, A. et al. Visualizing spatiotemporal dynamics of multicellular cell-cycle progression. *Cell* **132**, 487–498 (2008).
24. Liu, L., Michowski, W., Kolodziejczyk, A. & Sicinski, P. The cell cycle in stem cell proliferation, pluripotency and differentiation. *Nat. Cell Biol*. **21**, 1060–1067 (2019).
25. Vicente-Manzanares, M., Ma, X., Adelstein, R. S. & Horwitz, A. R. Non-muscle myosin II takes centre stage in cell adhesion and migration. *Nat. Rev. Mol. Cell Biol*. **10**, 778–790 (2009).
26. Gunning, P. W., Hardeman, E. C., Lappalainen, P. & Mulvihill, D. P. Tropomyosin - master regulator of actin filament function in the cytoskeleton. *J. Cell Sci*. **128**, 2965–2974 (2015).
27. Funk, J. et al. A barbed end interference mechanism reveals how capping protein promotes nucleation in branched actin networks. *Nat. Commun*. **12**, 5329 (2021).
28. Rotty, J. D., Wu, C. & Bear, J. E. New insights into the regulation and cellular functions of the ARP2/3 complex. *Nat. Rev. Mol. Cell Biol*. **14**, 7–12 (2013).
29. Hayashi, K. et al. Modulatory role of drebrin on the cytoskeleton within dendritic spines in the rat cerebral cortex. *J. Neurosci*. **16**, 7161–7170 (1996).
30. Serres, M. P. et al. F-actin interactome reveals vimentin as a key regulator of actin organization and cell mechanics in mitosis. *Dev. Cell* **52**, 210–222.e217 (2020).
31. Bernstein, B. W. & Bamburg, J. R. Actin-ATP hydrolysis is a major energy drain for neurons. *J. Neurosci*. **23**, 1–6 (2003).
32. Fujimura, L. et al. Protective role of Nd1 in doxorubicin-induced cardiotoxicity. *Cardiovasc. Res*. **64**, 315–321 (2004).
33. Mahammad, S. et al. Giant axonal neuropathy–associated gigaxonin mutations impair intermediate filament protein degradation. *J. Clin. Investig*. **123**, 1964–1975 (2013).
34. Hudson, A. M. & Cooley, L. Understanding the function of actin-binding proteins through genetic analysis of *Drosophila* oogenesis. *Annu Rev. Genet* **36**, 455–488 (2002).
35. Kim, I. F., Mohammadi, E. & Huang, R. C. C. Isolation and characterization of IPP, a novel human gene encoding an actin-binding, kelch-like protein. *Gene* **228**, 73–83 (1999).
36. Soltysik-Espanola, M. et al. Characterization of Mayven, a novel actin-binding protein predominantly expressed in brain. *Mol. Biol. Cell* **10**, 2361–2375 (1999).
37. Aromolaran, K. A., Benzow, K. A., Cribbs, L. L., Koob, M. D. & Piedras-Rentería, E. S. T-type current modulation by the actin-binding protein Kelch-like 1. *Am. J. Physiol. Cell Physiol*. **298**, C1353–C1362 (2010).
38. Heng, Y. W. & Koh, C. G. Actin cytoskeleton dynamics and the cell division cycle. *Int. J. Biochem. Cell Biol*. **42**, 1622–1633 (2010).
39. Jung, H.-J. et al. Regulation of prelamin A but not lamin C by miR-9, a brain-specific microRNA. *Proc. Natl. Acad. Sci. USA* **109**, E423–E431 (2012).
40. Gu, J. et al. ADF/cofilin-mediated actin dynamics regulate AMPA receptor trafficking during synaptic plasticity. *Nat. Neurosci*. **13**, 1208–1215 (2010).
41. Morrison, J. H. & Baxter, M. G. The ageing cortical synapse: hallmarks and implications for cognitive decline. *Nat. Rev. Neurosci*. **13**, 240–250 (2012).
42. Paquet, D. et al. Efficient introduction of specific homozygous and heterozygous mutations using CRISPR/Cas9. *Nature* **533**, 125–129 (2016).
43. Patro, R., Duggal, G., Love, M. I., Irizarry, R. A. & Kingsford, C. Salmon provides fast and bias-aware quantification of transcript expression. *Nat. Methods* **14**, 417–419 (2017).
44. Love, M. I., Huber, W. & Anders, S. Moderated estimation of fold change and dispersion for RNA-seq data with DESeq2. *Genome Biol*. **15**, 550 (2014).
45. Langfelder, P. & Horvath, S. WGCNA: an R package for weighted correlation network analysis. *BMC Bioinformatics* **9**, 559 (2008).
46. Wu, T. et al. clusterProfiler 4.0: a universal enrichment tool for interpreting omics data. *Innovation* **2**, 100141 (2021).
47. Heier, J. A., Dickinson, D. J. & Kwiatkowski, A. V. Measuring protein binding to f-actin by co-sedimentation. *J. Vis. Exp*. https://doi.org/10.3791/55613 (2017).
48. Cooper, J. A., Walker, S. B. & Pollard, T. D. Pyrene actin: documentation of the validity of a sensitive assay for actin polymerization. *J. Muscle Res. Cell Motil*. **4**, 253–262 (1983).
49. Yiangou, L. et al. Method to synchronize cell cycle of human pluripotent stem cells without affecting their fundamental characteristics. *Stem Cell Rep*. **12**, 165–179 (2019).

Acknowledgements

We would like to thank all members of Su-Chun's laboratories for their discussions and suggestions. We thank Andrew Petersen for technical help on CRISPR editing. F.Y. was supported by Duke-NUS Medical School Khoo Postdoctoral Fellowship (KPFA/2020/0038) and a National Medical Research Council Open Fund (OFYIRG22jul-0021). C.B. was supported by an NMRC Open Fund—Young Individual Research Grant (OF-YIRG/0048/2017). B.R is a fellow of the National Research Foundation (NRF, Singapore) and Branco Weiss Foundation (Switzerland) and an EMBO Young Investigator. This work was also funded by a Strategic Positioning Fund for Genetic Orphan Diseases (SPF2012/005) and an inaugural A*STAR Investigatorship from the Agency for Science, Technology and Research in Singapore to B.R.; S.-C.Z. was supported by Singapore Ministry of Education Research Fund (MOE2018-T2-2-103); Singapore Ministry of Health Research Fund (MOH-000207 and MOH-000212).

Author contributions

F.Y. conceived and designed the study, performed isogenic cell line generation, cell differentiation, immunostaining and imaging, immunoblots, data analysis and interpretation, and wrote the manuscript. Y.S.T. performed cell culture, immunostaining and imaging, immunoblots and data analysis. H.W. performed RNA-seq analysis. G.N. generated one pair of isogenic cell lines. L.Z. performed AP-MS experiments and proteomic data analysis. A.N.A., M.S., C.B., and B.R. provided the disease diagnosis, the patient's fibroblasts, and iPSCs. Q.Y., S.-M.C., and Y.-H.Y. performed data interpretation. S.-C.Z. conceived, designed and supervised the study, and wrote the manuscript. F.Y., Y.S.T., H.W., G.N., L.Z., A.N.A., M.S., C.B., B.R., Q.Y., S.-M.C., Y.-H.Y., and S.-C.Z. reviewed the manuscript. Correspondence should be addressed to S.-C.Z.

Competing interests

Su-Chun Zhang is a Co-founder of BrainXell, Inc. The remaining authors declare no competing interests.

Additional information

Supplementary information The online version contains supplementary material available at https://doi.org/10.1038/s41467-026-70756-x.

Correspondence and requests for materials should be addressed to Su-Chun Zhang.

Peer review information *Nature Communications* thanks the anonymous reviewers for their contribution to the peer review of this work. A peer review file is available.